Environmental Science Nano

Redox Chemistry of CeO_2 Nanoparticles in Aquatic Systems Containing Cr(VI)(aq) and Fe^{2+} Ions

Journal:	*Environmental Science: Nano*
Manuscript ID	EN-ART-02-2019-000201.R3
Article Type:	Paper
Date Submitted by the Author:	20-May-2019

Complete List of Authors:	Ray, Jessica; University of Washington, Civil & Environmental Engineering Wu, Xuanhao; Washington University in Saint Louis, Energy, Environmental & Chemical Engineering Neil, Chelsea; Los Alamos National Laboratory, Earth and Environmental Sciences Division Jung, Haesung; Georgia Institute of Technology, Earth and Atmospheric Sciences Li, Zhichao; Washington University, Department of Energy, Environmental and Chemical Engineering Jun, Young-Shin; Washington University, Energy, Environment and Chemical Engnieering

Environmental significance: Redox-active CeO_2 NPs are used in many industrial applications. Once CeO_2 NPs enter aquatic environments during or after use, these NPs may undergo subsequent redox reactions with coexisting redox-active species which may alter CeO_2 physicochemical properties and induce surface transformations. This work examines the fate and transport of CeO_2 NPs after redox reactions with Fe^{2+} and Cr(VI)(aq) species. The Cr(VI)(aq) enhanced formation of Fe(III) phases coated on CeO_2 NPs creating new hybrid, mobile, and less toxic nanomaterials.

Redox Chemistry of CeO_2 Nanoparticles in Aquatic Systems Containing Cr(VI)(aq) and Fe^{2+} Ions†

Jessica R. Ray[#], Xuanhao Wu, Chelsea W. Neil[‡], Haesung Jung[§], Zhichao Li, and Young-Shin Jun[*]

Department of Energy, Environmental & Chemical Engineering,
Washington University in St. Louis, St. Louis, MO 63130

Address: One Brookings Drive, Campus Box 1180
E-mail: ysjun@seas.wustl.edu
Phone: (314)935-4539
Fax: (314)935-7211
http://encl.engineering.wustl.edu/

Submitted: April 2019

Environmental Science: Nano

*To Whom Correspondence Should be addressed

[#]Current address: Department of Civil & Environmental Engineering, University of Washington, Seattle, WA 98195

[‡]Current address: Earth and Environmental Sciences Division, Los Alamos National Laboratory, Los Alamos, NM 87545, USA

[§] Current address: School of Earth and Atmospheric Sciences, Georgia Institute of Technology, Atlanta, GA 30332, USA

†Electronic supplementary information (ESI) available.

ABSTRACT

CeO_2 nanoparticles (NPs) are extensively used in industrial applications due to their high redox-catalytic activities and, as a result, may appear in aquatic environments where other redox-active species may coexist. To better predict the fate and transport of these nanomaterials, a comprehensive, mechanistic understanding of the physicochemical behaviors and transformation of CeO_2 NPs in complex, redox-active aqueous systems is needed. In this study, we investigated redox reactions of CeO_2 NPs with Fe^{2+} and Cr(VI) (i.e., model redox-sensitive species) at pH 5. We found that the co-existence of 0.1 mM Fe^{2+} and 1 (or 5) μM Cr(VI)(aq) promoted formation of Fe(III) (hydr)oxides and increased CeO_2 NP colloidal stability. Specifically, without Cr(VI), Ce^{3+}(aq) was rapidly released from the CeO_2/Fe^{2+} redox reaction, while the subsequent oxidation of Fe^{2+} to Fe^{3+} and formation of Fe(III) (hydr)oxides was slow. However, when Fe^{2+} and Cr(VI) coexist with CeO_2 NPs, the dissolution of CeO_2 NPs was slower than without Cr(VI), and Fe(III) (hydr)oxide precipitation on and near CeO_2 NPs significantly increased. The fast formation of Fe(III) (hydr)oxides can be attributed to facilitated Fe^{3+} hydrolysis by Cr(VI)(aq). Consequently, these new hybrid Fe(III)-CeO_2 NPs (i.e., CeO_2 NPs coated with Fe(III) phases) formed during redox-induced surface transformations exhibited a higher hydrophilicity, a more positive surface charge, and a greater colloidal stability compared to CeO_2 NPs in systems without Cr(VI). These findings reveal unexplored changes in surface chemistry and mobility of CeO_2 nanomaterials in complex redox-active aqueous systems.

INTRODUCTION

Cerium oxide (CeO_2) nanoparticles (NPs) are highly redox-active due to the number of oxygen vacancies in the lattice framework and defects at the NP surfaces,[1] allowing the CeO_2 NPs to easily shift between the 3+ and 4+ oxidation states.[2] Because they can act as both an oxidant and a reductant through environmentally adaptive electronic configuration changes, CeO_2 NPs lend their use to a wide variety of engineering applications, such as catalysis,[3, 4] additives in diesel fuels,[5-7] NO_x emission reduction in catalytic converters,[8, 9] chemical mechanical planarization,[10, 11] and thermal oxidation protection.[12, 13] Owing to these advances in catalytic CeO_2 technologies, CeO_2 NPs have become an emerging nanomaterial in natural and engineered aquatic systems. For example, Limbach et al. suggest that up to 6 mg/L of CeO_2 in a model wastewater treatment plant can exist in the effluent to pollute drinking source waters downstream.[14] Furthermore, CeO_2 NPs have been discovered in food crops, where they exhibit cytotoxicity to plant cells.[15-17] CeO_2 NPs also exhibit genotoxicity by increasing cellular reactive oxygen species concentrations and oxidative stress in human bronchial epithelial cells[18], causing DNA damage in human dermal fibroblasts,[19] and inducing apoptosis and autophagy in human peripheral blood monocytes.[20]

Both during and after their intended applications, the surface chemistry of CeO_2 NPs will evolve. Moreover, CeO_2 NPs will likely co-exist in systems with other redox-active species where they can undergo further transformations from unintended coupled redox reactions. As stated previously, CeO_2 NPs may exist in wastewater streams, or be released to the environment where they could enter drinking water sources and/or be taken up by plants in soil. Two potential redox-active species which can co-exist with CeO_2 NPs in these engineered and natural aquatic systems are Fe^{2+} and Cr(VI)(aq). For example, Ce^{4+}/Ce^{3+}, Fe^{3+}/Fe^{2+}, and/or Cr(VI)/Cr(III) co-exist in silicate glass preparation.[21, 22] Water used to cool unused molten glass can form a wastewater

stream that may contain dissolved Fe, Cr, and Ce species.[23] Additionally, stainless steel Fe–Cr alloys are often amended with small amounts of rare earth metals, like cerium, which significantly increase their oxidation resistance.[24] As a result, stainless steel leachate may contain Cr, Fe, and Ce to contaminate natural water sources.[25] Therefore, in addition to CeO_2 NPs emerging in natural aquatic systems to react with pre-existing Fe^{2+} and Cr(VI), the redox-active species we examined in this work can appear together in the same point source.

Furthermore, in natural aqueous environments, Fe^{2+} and Cr are ubiquitous and undergo constant geochemical cycling. Aqueous Fe^{2+} and Fe(II)-containing minerals such as pyrite, which are abundant in subsurface environments,[26-28] can reduce Cr(VI) to Cr(III).[29-32] Furthermore, Cr may exist in ground and surface waters discharged from industrial applications (e.g., leather tanning manufacturing).[33-36] Additionally, naturally occurring chromium[37-39] can exist in concentrations ranging from 0.02–50 μmol/g in soils.[40] Therefore CeO_2 NPs that bypass wastewater treatment to enter ground and surface waters can interact with these pre-existing redox-active species.

In this work, we built upon knowledge gained from our previous CeO_2–Fe^{2+} study[41] by investigating unexplored effects of Cr(VI)(aq) on CeO_2 NP surface properties in the presence of Fe^{2+} ions. Our previous research suggests that CeO_2 NP-Fe^{2+} interactions will promote secondary solid phase formation owing to sorption of Fe^{2+} onto CeO_2 and subsequent redox reactions. With the addition of Cr(VI) in the CeO_2 NP-Fe^{2+} system, Fe^{2+} sorption and transformation by CeO_2 NPs can be significantly altered, and the homogeneous Fe^{2+}-Cr(VI) redox reactions can also be affected. Thus, it is important to investigate this tertiary system because these redox-active species can: (1) induce physicochemical changes and surface transformation of CeO_2 NPs; (2) form new, hybrid nanoscale particle phases with new surface reactivities; and (3) affect the fate and transport

of CeO_2 NPs in natural and engineered aquatic systems. To examine these effects, we have performed a series of complementary experiments to systematically elucidate the redox reaction mechanisms occurring on surfaces of CeO_2 NPs as well as competing redox reaction pairs between CeO_2/Fe^{2+} and Fe^{2+}/Cr(VI). Results from this work provide valuable insight into the phase transformation and colloidal stability of CeO_2 NPs in complex, redox-active aquatic environments.

MATERIALS AND METHODS

Chemicals and Materials. All chemicals used were at least ACS grade. Suspensions of commercial CeO_2 NPs (Sigma Aldrich, MO) were reacted with solutions of ferrous chloride ($FeCl_2 \cdot 9H_2O$; JT Baker, PA) for Fe^{2+} and/or potassium dichromate ($K_2Cr_2O_7$; JT Baker, PA) for Cr(VI)(aq). We chose to use commercially available CeO_2 NPs so that our results are more closely connected to real engineered NPs and are more comparable to other studies that used similar particles. CeO_2 NPs were characterized using wide-angle X-ray diffraction (WAXRD, 58.66 keV, Figure S1) in sector 11-ID-B at the Advanced Photon Source (APS) at Argonne National Laboratory (IL, USA). The surface area of the NPs was measured by the Brunauer–Emmett–Teller method (BET, NOVA 2000e) to be 48.34 m^2/g. A 10 mM sodium chloride (NaCl; BDH, PA) was used to maintain the same ionic strength in each system.

Sedimentation and Dissolution Experiments. To study the effect of Cr(VI) on CeO_2–Fe^{2+} interactions, "**CeO_2**", "**CeO_2+Fe^{2+}**", "**CeO_2+5Cr(VI)**" systems were used as controls and there were two reaction systems: "**CeO_2+Fe^{2+}+Cr**" and "**CeO_2+Fe+5Cr**". Prior to the experiments, a 50 mg/L CeO_2 stock solution was prepared using deoxygenated water and sonicated for 1 h inside an anaerobic chamber. One hour sonication (Fisher Scientific ultrasonicator model no. FS6 with a frequency of 50/60 kHz and power of 30W) allowed time for aggregates to break up and for the CeO_2 NPs to equilibrate with the deoxygenated

water. After sonication, aliquots of the CeO_2 NP stock solution were added to 50 mL test tubes with 10 mM NaCl. To initiate the reactions, the solutions were made to contain 1×10^{-4} M Fe^{2+} and/or 1 (or 5) $\times 10^{-6}$ M Cr(VI) (referred as Cr (or 5Cr)). The **CeO_2+Fe^{2+}+5Cr** system was tested to determine the effects of higher Cr(VI) concentrations on CeO_2 NPs' chemical and physical stability. The concentrations of each of the reaction constituents are given in Table S1 in the Electronic Supplementary Information (ESI). The Fe^{2+} concentrations are relevant to typical concentrations used during wastewater coagulation pretreatment (0.05–0.5 mM)[42-46] and in groundwater (0.001–2 mM)[47-51]. Similarly, Cr(VI) concentrations are in the range of those in wastewater effluents (0.1–20 μM)[52-56] and groundwater (1–100 μM)[57-59]. The pH of the stock reactant solutions were all ~pH 5 before mixing to start the reaction.

To evaluate CeO_2 NPs' colloidal stability, sedimentation experiments were conducted. For sedimentation and dissolution experiments as well as all subsequent experiments employing both Fe^{2+} and Cr(VI) ions, Fe^{2+} was added to the CeO_2-containing system first, followed by immediate addition of Cr(VI). Once **CeO_2**, **CeO_2+Fe^{2+}**, **CeO_2+Fe^{2+}+Cr**, and **CeO_2+Fe^{2+}+5Cr** systems were prepared, the test tubes were capped and mixed by shaking vigorously for 15 seconds. At hourly intervals for a total of 6 h, 1 mL from each solution was pipetted into cuvettes for UV-Vis spectrophotometry (Agilent Cary® 50 UV-Vis, CA) analysis. To better determine the CeO_2 NPs' settlement in each system, the 1 mL sample was taken at the top 5 mL of the 50 mL test tube to avoid collecting large aggregates near the middle and bottom of the test tube. The cuvettes were then capped, wrapped with Teflon tape to prevent gas transfer, and removed from the Coy anaerobic chamber to measure the absorbance of CeO_2 NPs using UV-Vis at 305 nm. The 305 nm wavelength was confirmed in our previous study to indicate the absorption peak for CeO_2 NPs.[41, 60] To relate the particle size of CeO_2 NPs in each system to their sedimentation, dynamic light

scattering (DLS, Malvern 1011155 Zetasizer Nanoseries, MA) was used to measure the hydrodynamic particle size of CeO_2 NPs or heterogeneous aggregates in each reaction system.

For CeO_2 NP dissolution experiments, solutions were prepared in 50 mL test tubes as before, then divided into 5 mL test tubes for mixing in a rotator throughout the sampling period. Each hour, samples from the 5 mL test tubes were transferred to ultracentrifuge tubes in the chamber, capped, and ultracentrifuged (Thermo Scientific Sorvall WX Ultra Series) at 40,000 rpm for 45 min. After ultracentrifugation, the tube was placed back in the Coy chamber, filtered using a 0.2 μm syringe filter, then acidified to 2% v/v nitric acid for inductively coupled plasma-mass spectrometry (ICP-MS, Agilent 7500ce, CA) aqueous Ce measurements. The hydrodynamic diameter of CeO_2 NP aggregates was around 1 μm (DLS, Figure S2); therefore, ICP-MS analysis should be of aqueous cerium only. Triplicate measurements were conducted for both sedimentation and dissolution experiments.

While CeO_2–Fe^{2+}–Cr(VI) interactions are more likely to occur in aerobic aquatic environments, it is important to separate out the effects of dissolved oxygen (DO) to better elucidate the redox reaction mechanisms among CeO_2, Fe^{2+}, and Cr(VI) in our systems. Thus, the majority of experiments were conducted under anaerobic conditions in a Coy chamber (i.e., P_{O_2} = 0 atm), where all solutions and aqueous-based experiments were prepared using deoxygenated water. For comparison, however, **CeO_2+Fe^{2+}** and **CeO_2+Fe^{2+}+Cr** dissolution and sedimentation experiments were also conducted under aerobic conditions to check potential DO effects.

Heterogeneously Formed Secondary Mineral Phase Identification. To systematically study heterogeneous precipitation in experimental systems, CeO_2-sputtered Si wafers ("CeO_2 wafer") were prepared by depositing CeO_2 NPs onto Si (111) wafers via physical vapor deposition

(Kurt Lesker PVD 75, CA). Si wafers were first cleaned with acetone and DI water, dried with nitrogen gas, and stripped of their native oxide layer using buffered oxide etch solution (Transene Company, Inc., MA) for 3 min. During the physical vapor deposition (PVD) process, DC (diode) mode was applied under 1 mTorr argon pressure, with 100 watts power input to the CeO_2 source for 2000 seconds. The deposition was monitored in situ via a built-in quartz crystal microbalance.

To prepare heterogeneously formed precipitates on the CeO_2 surface, the CeO_2 sputtered wafer was cut into a 1 cm × 1 cm coupon and placed at the bottom of a cuvette. The cuvette was then transferred into the anaerobic chamber to prevent the influence of DO. Triplicate coupons for each of the two **CeO_2** and **CeO_2+Fe^{2+}** control systems and two reaction (**CeO_2+Fe^{2+}+Cr** and **CeO_2+Fe^{2+}+5C**r) systems were then reacted under the same aqueous chemistry as the reaction systems in the sedimentation and dissolution experiments. To minimize the accumulation of homogeneously formed precipitates on the coupon by gravitational settling, the cuvettes were inverted so that the coupon was on top of the solution and there was no discernible air gap between the solution and the coupon. After 1 h of reaction, the coupons were removed from the cuvette, rinsed with deoxygenated DI water, and then allowed to dry in the anaerobic chamber overnight.

To visualize precipitates, the coupon topographies were analyzed with tapping mode atomic force microscopy (AFM, Veeco Multimode). The probes were 125 μm long, with phosphorus (n) doped silicon tips (a nominal tip radius of 10 nm, MPP-11100-10, Veeco probes). The images were collected with drive frequencies of 312–320 kHz, typical spring constants of 20–80 N/m, scan sizes of 3 μm × 3 μm, and scan rates of around 0.80–1.0 Hz. The surface roughness was measured using Nanoscope® 7.20 software over a scan area of 2 μm × 2 μm. To characterize the surface chemistries and oxidation states of precipitates, X-ray photoelectron spectroscopy (XPS, PHI 5000 VersaProbe II, Ulvac-PHI) was used to measure Fe 2p, Cr 2p, O 1s, and Ce 3d spectra

on the dried CeO_2 coupons. An Al Kα monochromator radiation at a passing energy of 1486.6 eV was used to collect the spectra, and Multipack (V7.0.1, Ulvac-PHI, Inc.) was used to fit the data using the Gaussian-Lorentzian fitting function. The peak positions used in the Gaussian-Lorentzian fit for O 1s, Fe 2p, and Ce 3d are given in Table S2, S3, and S4.

Homogeneously Formed Secondary Mineral Phase Identification. Several complementary analytical techniques were performed to identify secondary phases: High resolution transmission electron microscopy (HR-TEM, JEOL 2100F) electron diffraction (ED), X-ray absorption spectroscopy (XAS, sector 13-BM-D, Argonne National Laboratory), and diffuse reflectance infrared Fourier transform spectroscopy (DRIFTS, Praying Mantis accessory, Harrick Scientific). For HR-TEM analysis, approximately 50 μL of experimental solution was placed on 300-mesh Cu Formvar-carbon grids to dry before analysis. HR-TEM and AFM were used to observe secondary mineral phase formation before and after reaction. ED patterns collected during HR-TEM analysis were used to identify secondary mineral phases on and near CeO_2 NPs. For AFM analysis, the cuvettes containing the CeO_2-sputtered coupons and experimental solutions were not inverted to better observe the contribution of homogeneously nucleated precipitates along with heterogeneously formed precipitates. To prepare solid samples for DRIFTS and XAS, larger volumes of the same CeO_2 NP suspensions used in the sedimentation and dissolution experiments were prepared. As before, the solutions were ultracentrifuged and returned to the anaerobic chamber, where the supernatant was removed and the accumulated powder at the bottom of the ultracentrifuge tube was allowed to dry for 2–3 days in the chamber. For DRIFTS analysis, the samples were diluted 10 times (by mass) with potassium bromide powder. For XAS, the Ce K-edge was measured in transmission mode while the Fe and Cr K-edges were measured in fluorescence mode. Fluorescence mode is needed for Fe and Cr because it is more surface-

sensitive, and can thus detect the trace Fe and Cr phases compared to bulk CeO_2. A Si (111) monochromator gave a focused beam size of 10 μm × 30 μm and a resolution of 1×10^{-4} ΔE/E. The energy flux was 1×10^9 at 10 keV. The energy range for this station was 4.5–70 keV. The Fe K-edge in X-ray absorption near edge structure (XANES) was measured at 7.119 keV, the Ce K-edge at 40.444 keV, and the Cr K-edge at 5.989 keV. To provide insight into the differences of secondary phase physicochemical properties, thermogravimetric analysis (TGA) and the corresponding differential thermogravimetric analysis (DTA) were also performed on a TGA Q5000 (V3.17 Build 265) in nitrogen with a ramp of 15 °C/min.

Electrophoretic Mobility and Aqueous Fe^{2+} and Cr(VI) Concentration Determination. To further investigate redox reaction mechanisms and to characterize changes in aqueous chemistry during the reaction, additional aqueous chemistry measurements were performed. In addition to the changes in system pH, we monitored the electrophoretic mobility evolution of the CeO_2 NPs throughout the 6 h reaction period using a Zetasizer (Malvern 1011155 Zetasizer Nanoseries, MA).

To determine changes in Fe^{2+} and Cr(VI) aqueous concentrations resulted from redox reactions and/or sorption onto CeO_2 NPs, the aqueous concentrations of Fe^{2+} and Cr(VI) in the presence and absence of CeO_2 were quantified by the ferrozine[61] and diphenylcarbazide (DPC) colorimetric methods.[62] The solutions for the **CeO_2+Fe^{2+}, CeO_2+Fe^{2+}+Cr,** and **CeO_2+Fe^{2+}+5Cr** systems were prepared in 50 mL test tubes inside the anaerobic chamber as before. After 6 h of reaction, the suspensions were ultracentrifuged and filtered using a 0.2 μm syringe filter as before. To measure aqueous Fe^{2+} concentrations, 0.1 mL of each of the filtered solutions was added to 5 mL of ferrozine solution, and ferrozine absorbance was measured using UV-Vis spectrophotometry at 562 nm. The ferrozine solution was prepared by dissolving 1 g of ferrozine

(J.T. Baker, PA) in 1 L of 50 mM HEPES buffer at pH 7 (prepared in the anaerobic chamber using deoxygenated water). To measure the aqueous Cr(VI) concentrations, the DPC method was used: 100 µL of DPC solution (250 mg of DPC in 50 mL acetone) and 500 µL of 10% v/v H_2SO_4 were added to 5 mL of the filtered solutions containing Cr(VI), and DPC absorbance was measured using UV-Vis spectrophotometry at 540 nm. To determine the extent of Fe^{2+} oxidation and Cr(VI) reduction in the absence of CeO_2 NPs, the same condition solutions were prepared in the anaerobic chamber without CeO_2, and the ferrozine and DPC methods were employed as before. Triplicate tests were conducted. Additional experimental details are given in the ESI.

RESULTS AND DISCUSSION

Co-existing Fe^{2+} (aq) and Cr(VI)(aq) Enhance the Colloidal Stability of CeO_2 NPs and Inhibit the Dissolution of CeO_2 NPs. Under anaerobic conditions, CeO_2 NP colloidal stability increased in the order: **CeO_2** < **CeO_2+Fe^{2+}** < **CeO_2+Fe^{2+}+Cr** < **CeO_2+Fe^{2+}+5Cr** (Figure 1A). Nearly 80% of CeO_2 NPs in the **CeO_2+Fe^{2+}+5Cr** system remained in suspension after 6 h of reaction, while only 20% remained suspended in the **CeO_2** system. Compared to our previous study at a higher Fe^{2+} concentration (3 mM $FeCl_2$),[41] the lower 0.1 mM Fe^{2+} concentration in the **CeO_2+Fe^{2+}** system used in this study only slightly improved colloidal stability compared to the **CeO_2** control system. This data suggests that increased Cr(VI) concentrations in Fe^{2+}-containing systems may promote reactions near the CeO_2 NP surface that increase CeO_2 colloidal stability. The DLS hydrodynamic particle size measurements (Figure S2E) were consistent with settlement results, in that the **CeO_2+Fe^{2+}+5Cr** system had the smallest aggregate size (and highest colloidal stability), while the **CeO_2** and **CeO_2+Fe^{2+}** systems exhibited larger aggregate sizes and more

sedimentation. The **CeO_2+5Cr** control displayed the fastest sedimentation (Figure 1A) and the largest aggregate size (Figure S2E).

Under anaerobic conditions, while Fe^{2+} and Cr(VI)(aq) containing systems significantly promoted CeO_2 NP colloidal stability, the dissolution of CeO_2 NPs was drastically inhibited in those systems (Figure 1B). Because the solubility of $Ce^{IV}O_2$ is negligible compared to Ce^{III} (hydr)oxide (i.e., $K_{sp} = 5.0 \times 10^{-60}$ for $Ce^{IV}O_2$,[63] and $K_{sp} = 1.6 \times 10^{-20}$ for $Ce(OH)_3$),[64, 65] we can assume that the dissolved Ce was in the 3+ oxidation state at our system pH. The **CeO_2+Fe^{2+}** system exhibited the greatest dissolution, releasing over 14 times more Ce^{3+} than the **CeO_2** system. Because CeO_2 dissolution (i.e., **CeO_2** system) is negligible (Figure 1B), particularly compared to when Fe^{2+} is introduced (i.e., **CeO_2+Fe^{2+}** system), the oxidation of Fe^{2+} could occur after sorption of Fe^{2+} onto CeO_2 NPs rather than after oxidation by aqueous Ce^{3+} ions. The **CeO_2+Fe^{2+}+Cr** reaction system had the second highest dissolution releasing twice as much Ce^{3+} as the **CeO_2** system, followed by the **CeO_2+Fe^{2+}+5Cr** system which exhibited the same dissolution as the **CeO_2** system.

To test the effects of DO on CeO_2 NP sedimentation and dissolution, **CeO_2+Fe^{2+}** and **CeO_2+Fe^{2+}+Cr** systems were examined. In particular, these two systems were chosen because they exhibited clear differences in both sedimentation and dissolution in the anaerobic experiments. The presence of DO significantly enhanced colloidal stability in both systems, resulting in only 17% settlement in the **CeO_2+Fe^{2+}** system at 6 h, compared to 52% in the absence of DO (Figure 1A, dashed lines). In the **CeO_2+Fe^{2+}+Cr** system at 6 h, there was 30% more suspended CeO_2 colloids when DO was present. In the presence of DO, the measured aqueous Ce^{3+} in the **CeO_2+Fe^{2+}** system was 6 times less than the Ce^{3+} released under anaerobic conditions (Figure 1B, dashed lines). This effect of DO on CeO_2 dissolution was less severe in the

CeO_2+Fe^{2+}+Cr system. Because the DO resulted in a significant enhancement of colloidal stability and simultaneous inhibition of Ce^{3+} dissolution, to delineate the redox chemistry mechanisms among CeO_2, Fe^{2+}, and Cr(VI), we pursued a more detailed systematic investigation under anaerobic conditions.

To relate CeO_2 NP surface chemistry changes and reaction mechanisms to changes in aqueous chemistry, the pH and zeta potential were measured after the initial mixing of the reaction species (roughly 10 min after reaction), and after 6 h of reaction. The zeta potential of the CeO_2 NPs measured in 10 mM NaCl at pH 5 was 16 mV (Figure 1) and the zeta potential of the **CeO_2+Fe^{2+}** system was even higher (28 mV). This suggests that the Fe^{2+} ions adsorbed to positively charged CeO_2 NP surfaces despite repulsive electrostatic interactions.[66] It is important to note that the surface potential of the bare CeO_2 in NaCl system was tested at least 20 times with several batches of commercial CeO_2 powders (from Sigma Aldrich, MO) and high variability in zeta potential was observed in the pH 5–7 range. In this pH range, the measured zeta potential of the bare CeO_2 NP powders varied by ± 15 mV depending on the age of the commercial CeO_2 powders, the history of exposure to oxygen, and the background electrolyte type used for surface potential measurements. However, once Fe^{2+} and Cr(VI) metal ions were added to the reaction mixture, the zeta potential measurements became highly stable and reproducible over five separate tests (in triplicate per test). The pH of the CeO_2, Fe^{2+}, and Cr(VI) stock solutions were pH 5 ± 0.1 prior to mixing. After 10 min of reaction, the pH of the **CeO_2+Fe^{2+}+Cr** and **CeO_2+Fe^{2+}+5Cr** systems decreased from 5.0 to 4.8 and 4.6, potentially due to Fe^{3+} hydrolysis or the adsorption of Fe^{2+} onto CeO_2 surface through ion exchange.[41] The pH drop coincided with increased zeta potentials on CeO_2 NP surfaces, from 16.2 mV (in the **CeO_2** control system) to 29.0 mV and 31.0 mV in the **CeO_2+Fe^{2+}+Cr** and **CeO_2+Fe^{2+}+5Cr** systems. This indicates that Cr(VI) facilitated reactions with

Fe^{2+} that significantly increased the CeO_2 NP surface potential because simple adsorption of Cr oxyanions on CeO_2 NPs can only decrease the surface potential. In addition to Cr(VI)-facilitated Fe^{2+} transformation on and near CeO_2 NPs, Cr(VI) may also sorb onto the CeO_2 NPs. For example, in the **CeO_2+5Cr** control system, the addition of Cr(VI) resulted in a 12.5 mV decrease in the CeO_2 surface charge.

Cr(VI)(aq) Increases the Extent of Heterogeneous and Homogeneous Secondary Solid Phase Formation. HR-TEM micrographs revealed the extent of secondary solid phase formation on and near the CeO_2 NPs in each reaction system (red arrows in Figure 2). As the Cr(VI) concentration increased, there was a clear increase in the amount of precipitates (Figure 2C and 2D). The increase in secondary solid phase formation can also be observed in the AFM images for the non-inverted configuration (Figure S3, row 2). The HR-TEM electron diffraction analysis performed on the **CeO_2+Fe^{2+}**, **CeO_2+Fe^{2+}+Cr**, and **CeO_2+Fe^{2+}+5Cr** systems of new phases attached to CeO_2 NPs identified 6-line ferrihydrite (6LF) as the Fe(III) phase formed (Figure S3). For the Cr(VI)-containing reaction systems, no Cr(III) (or Cr(VI)) solid phase was identified in the **CeO_2+Fe^{2+}+Cr** system; however, eskolaite (Cr_2O_3) was identified in the **CeO_2+Fe^{2+}+5Cr** system. There is a caveat that drying effects during the HR-TEM sample preparation might promote phase transformation to more thermodynamically stable phases. Therefore, we can expect that the Fe(III) and Cr(III) phases that form in solution are poorly crystalline, hydrous phases (i.e., $Fe(OH)_3$ and $Cr(OH)_3$). A complementary XPS analysis of heterogeneous secondary solid phases from the inverted CeO_2 coupon test also confirmed the formation of both Fe- and Cr-containing precipitates (Figure 3A and 3B). The peak locations and their corresponding elemental composition match with references for O 1s, Fe 2p, and Ce 3d spectra are given in Tables S2, S3, and S4. Ce 3d XPS peaks (Figure S7A) indicate that the presence of Fe^{2+} increased the Ce(III)%

on CeO_2 NP surfaces, which resulted from the Ce^{IV}/Fe^{2+} redox reaction. Furthermore, the XPS result of the **CeO_2+Fe^{2+}** system is consistent with the dissolution results, in that highest amount of Ce(III) formed both on the surface and in the solution. This finding suggests that Ce^{IV} could be reduced to Ce^{III} by Fe^{2+} on the CeO_2 NP surface, and the subsequent formation of Ce^{3+} was released into solution. With increasing Cr(VI) concentration, the Fe^{2+}/Fe^{3+} ratio decreased, suggesting more Fe(III) phases formed on the CeO_2 NP surfaces. [67-6967-69] Similarly, the Fe/Ce ratio increases with increasing Cr(VI) concentration, which supports our experimental observations of larger extents of Fe^{3+} phase formation on CeO_2 NP surfaces with the addition of Cr(VI). Note that the CeO_2 XPS spectra appears to contain peaks in the Fe 2p spectra binding energy range (716.1 and 732.3 eV). The XPS survey scan for sputtered CeO_2 (Figure S5), as well as reports by Krawczyk et al.,[70] indicate that Ce 3d contributed two peaks which overlap with Fe 2p peaks in lower energy ranges. The areas of the Fe-related peaks over the Ce peaks were used to calculate the Fe/Ce ratios shown in Table S3. On the other hand, Cr 3d XPS analysis of the heterogeneously nucleated particles (Figure 3B) shows Cr $2p_{1/2}$ and $2p_{3/2}$ peaks of 586.2 and 576.6 eV which correspond to Cr(III) phases on the CeO_2 NP surface.[71]

Bulk phase analysis of homogeneously formed precipitates revealed additional information regarding secondary Fe(III) and Cr(III) solid phases in each reaction system. As observed in the Fe 2p XPS data for heterogeneous precipitates, the Fe K-edge XAS (Figure S6A) and DRIFTS (Figure S6B) of newly formed hybrid NPs in solution also show increasing extents of 6LF formation in the order: **CeO_2+Fe^{2+}** $\leq$ **CeO_2+Fe^{2+}+Cr** < **CeO_2+Fe^{2+}+5Cr**. This is consistent with changes in the zeta potential and pH values (table adjoining Figure 1). Hydrolysis of Fe^{3+} and consequential formation of 6LF will decrease pH and increase zeta potential of the NP surface to be more positive, as shown in the following equation: $Fe^{3+} + 3H_2O \leftrightarrows Fe(OH)_{3(s)} + 3H^+$.[72, 73] The

largest pH drop in the **CeO_2+Fe^{2+}+5Cr** system (pH 5 to pH 4.33 in 6 h) was due to the highest extent of iron hydrolysis, which is in agreement with observations of the highest extent of bulk and heterogeneous 6LF formation. Heterogeneous Fe(III) (hydr)oxide precipitates may help to increase the colloidal stability of CeO_2 by increasing the surface charge and hydrophilicity of NPs.[41] The concurrent pH decrease, zeta potential increase, and formation of heterogeneous Fe(III) phases can explain our observed trends of high colloidal stability for the **CeO_2+Fe^{2+}+Cr** and **CeO_2+Fe^{2+}+5Cr** reaction systems. Similarly, in the **CeO_2+Fe^{2+}** system, the smallest magnitude in pH decrease, and the smallest increase in zeta potential and extent of heterogeneous Fe(III) formation could explain why the colloidal stability for **CeO_2+Fe^{2+}** system was relatively low.

Cr(III) phases were also identified in Cr(VI)-containing systems by several mineral phase identification techniques. In the **CeO_2+Fe^{2+}+Cr** system, the Fourier-transformed Fe K-edge XAS spectrum exhibited an additional coordination (enclosed in the red box, Figure 3C) not associated with 6LF. The literature suggests this coordination corresponds to an $Fe^{III}_xCr^{III}_{(1-x)}(OH)_3$ (or a mixed Fe(III)-Cr(III) hydroxide) phase,[74] which has also been reported in similar systems investigating Fe^{2+}-Cr(VI) redox reactions.[75] For example, Hansel et al. used Fe XAS to confirm the presence of an $Fe_{0.67}Cr_{0.33}(OH)_3$ phase, which was produced from Cr(VI) reduction by iron-reducing bacteria under anaerobic conditions.[74] Similarly, Eary and Rai observed $Cr_x(Fe_{1-x})(OH)_3$ phases while investigating the reduction of Cr(VI) by Fe(II) at pH 5 under anaerobic conditions.[75] In the **CeO_2+Fe^{2+}+5Cr** system, however, we suggest that distinct $Fe(OH)_3$ and $Cr(OH)_3$ phases form during reaction based on the XPS and TGA-DTA analysis. Elemental XPS calculations give –OH and H_2O contributions in the **CeO_2+Fe^{2+}+Cr** and **CeO_2+Fe^{2+}+5Cr** systems from the O1s XPS spectra (Figure S6B and Table S2). In the **CeO_2+Fe^{2+}** system, the percentage of –OH groups significantly increased, suggesting the formation of $Fe(OH)_3$ phases on CeO_2 surfaces. On the

other hand, the H_2O peak significantly increased for the **CeO_2+Fe^{2+}+Cr** and **CeO_2+Fe^{2+}+5Cr** systems, which may be attributed to the formation of hydrated mixed Fe(III)-Cr(III) and Cr(III) phases. TGA-DTA analysis (Figure 4) also supports our hypothesis. The DTA exothermic peak at 800°C (marked in Figure 4B) indicates the crystallization of amorphous (i.e., hydroxide or hydrous) phases in the **CeO_2+Fe^{2+}+Cr** and **CeO_2+Fe^{2+}+5Cr** systems.[76] The exothermic peak was negligible in the **CeO_2** and **CeO_2+Fe^{2+}** spectra due to the low extent of hydrous secondary phase formation in these systems. In the two reaction systems containing Cr(VI), the exothermic peak appeared significantly larger in the **CeO_2+Fe^{2+}+Cr** spectra than in the **CeO_2+Fe^{2+}+5Cr** spectra. This could be owing to the highly amorphous $Fe^{III}_xCr^{III}_{(1-x)}(OH)_3$ phase compared to the more crystalline $Fe(OH)_3$ and $Cr(OH)_3$ phases present in the **CeO_2+Fe^{2+}+5Cr** system.

Competing Redox Reactions among CeO_2 NP, Fe^{2+}, and Cr(VI) Promote Solid Fe(III) Formation on CeO_2 NPs and their Aggregates. The hydrolysis of Fe^{3+} in our experimental systems was enabled by the redox reactions of Fe^{2+}/Cr(VI) and Ce^{IV}/Fe^{2+} pairs:

$$3Fe^{2+} + HCrO_4^- + 7H^+ \leftrightarrows 3\ Fe^{3+} + Cr^{3+} + 4H_2O \qquad E^\circ_{rxn} = 0.43\ V \qquad (1)$$

$$Ce^{(IV)}O_2 + Fe^{2+} + 4H^+ \leftrightarrows Ce^{3+} + Fe^{3+} + 2H_2O \qquad E^\circ_{rxn} = 2.05\ V \qquad (2)$$

where the standard reduction potentials are Fe^{3+}/Fe^{2+}(0.77 V),[77] Ce(IV)/Ce^{3+}(2.82 V),[78, 79] and $HCrO_4^-/Cr^{3+}$(1.20 V).[77] Detailed redox and cell potential calculations are available in the ES1. Based on our calculations using the Visual MINTEQ software[80], at our initial system pH of 5, the dominant Cr(VI) species should be the $HCrO_4^-$(aq) species. Visual MINTEQ was then used to determine the electrochemical potentials for reactions (3)–(5) for Fe(III) solid formation by $HCrO_4^-$ and CeO_2. The Gibbs free energies were then calculated based on the modeled electrochemical potentials.

ΔG_{rxn} (pH = 5, **Fe^{2+}+Cr** system) = -128.48 kJ; (3)

ΔG_{rxn} (pH = 5, **Fe^{2+}+5Cr** system) = -139.77 kJ; and (4)

ΔG_{rxn} (pH = 5, **CeO_2+Fe^{2+}** system) = -39.31 kJ (5)

Oxidation of Fe^{2+} is highly favored in reaction systems containing Cr(VI)(aq), particularly in the system containing higher Cr(VI) concentrations. The Ce^{IV}/Fe^{2+} redox reaction is still thermodynamically favorable to form Fe^{3+}, but there is as lower thermodynamic driving force compared to the Fe^{2+}/Cr(VI) pair. According to Visual MINTEQ modeling, Fe(III) phases were all supersaturated with respect to ferrihydrite with the **Fe^{2+}+5Cr** system exhibiting the largest degree of supersaturation. This finding is consistent with our experimental secondary phase formation results.

Ferrozine and DPC colorimetric analyses provided further information about the effect of CeO_2 on the extent of Fe^{2+} oxidation by Cr(VI)(aq) species. Table 1 provides the amount of Fe^{2+} remaining in the system solutions after 6 h of reaction. To better determine the effect of CeO_2 NPs on the redox chemistry, experiments were performed in the presence and absence of CeO_2 for both ferrozine and DPC analyses. The redox reaction between Fe^{2+} and Cr(VI) occurs readily (Table 1 and Table 2), is thermodynamically favorable (Equation 3 and 4), and induces secondary mineral phase formation. The ferrozine (Table 1) and DPC (Table 2) results for the homogeneous Fe^{2+} and Cr(VI) reaction system in the absence of CeO_2 NPs can provide insights into the amount of secondary phase formation occurring via redox reactions. In the presence of CeO_2 NPs, the extent of Fe^{2+} oxidation and/or removal was enhanced and Cr(VI) reduction and/or removal was increased to a lesser extent. For example, in the **Fe+Cr** system, 30% more Fe^{2+} was transformed

(i.e., oxidized) or removed (i.e., adsorbed) when CeO_2 NPs were introduced (Table 1). Similarly, Cr(VI) was completely reduced or adsorbed in the **Fe+5Cr** system in the presence of CeO_2 NPs. Therefore, even if Fe^{2+} and Cr(VI) co-exist in natural or engineered aqueous environments and undergo redox reactions prior to exposure to CeO_2 NPs, emerging CeO_2 NPs can significantly impact the redox chemistry and reactivity by acting as reactive media.

For aqueous Fe^{2+} measurements, it is important to note that the amount of Fe^{2+} remaining after reaction can be influenced by multiple processes: (1) sorption of Fe^{2+} onto CeO_2, (2) oxidation of Fe^{2+} by CeO_2 and/or Cr(VI), and (3) precipitation of 6LF and/or the Fe(III) and/or Cr(III) hydroxide phases. This suggests that CeO_2 can serve as an Fe^{2+} oxidizer (or adsorbent) even in the absence of Cr(VI), which we can observe indirectly from the rapid release of aqueous Ce^{3+} (from the Ce^{4+}/Fe^{2+}) redox reaction over the 6 h period in the **CeO_2+Fe^{2+}** (Figure 1B) system and from the thermodynamic calculations. The further addition of Cr(VI) promoted Fe(III) secondary solid phase formation on or near the CeO_2 NP surface (Figure 2, 3A and 3B), which also suggests that Fe^{2+} sorption onto CeO_2 NPs is occurring in our system. The Fe^{3+} formation on or near the CeO_2 NP surface for this system may be thermodynamically favorable and kinetically fast (i.e., rapid release of Ce^{3+} seen in Figure 1B); however, the subsequent hydrolysis of aqueous Fe^{3+} to form solid Fe(III) phases may be slow (particularly at our initial system pH 5)[81] as we observed the lowest extent of heterogeneous (and homogeneous) Fe(III) solid phases formed in the **CeO_2+Fe^{2+}** system (Figure 3A).

When Cr(VI) was added, 80% and 100% of measurable aqueous Fe^{2+} was oxidized in the **CeO_2+Fe^{2+}+Cr** and **CeO_2+Fe^{2+}+5Cr** systems according to the Ferrozine method analysis (Table 1). In these systems, the extent of heterogeneous 6LF nucleation (as indicated by XPS analysis) from hydrolysis of sorbed Fe^{2+} oxidation was significantly larger than in the **CeO_2+Fe^{2+}** system,

which suggests that the Fe^{3+} hydrolysis reaction is kinetically favored when Cr(VI) is present. The Cr(VI)(aq) remaining at the end of the 6 h reaction period was negligible (DPC detection limit: 1×10^{-8} M) for all reaction systems (with and without CeO_2), indicating that all the Cr(VI) was reduced and mineralized, forming the $Fe^{III}_xCr^{III}_{(1-x)}(OH)_3$ or $Cr(OH)_3$ phases.

CONCLUSIONS

In this study, we demonstrated the intricate redox reactions and CeO_2 NP surface transformations that can occur when CeO_2 NPs and redox-active species Fe^{2+} and Cr(VI)(aq) coexist in aqueous environments. Our results show that increased concentrations of Cr(VI)(aq) promoted colloidal stability and inhibited dissolution of CeO_2 NPs when Fe^{2+} was present. High concentrations of Cr(VI)(aq) promoted the formation of distinct $Fe(OH)_3$ and $Cr(OH)_3$ phases on the CeO_2 NP surface, while lower concentrations generated a $Fe^{III}_xCr^{III}_{(1-x)}(OH)_3$ solid solution phase on the surface. The Fe(III)-containing surface coating formed on CeO_2 NPs and aggregates may alter the native CeO_2 NP reactivity and facilitate sorption of additional contaminants if these hybrid particles are released to downstream in the environment. Furthermore, our DPC analysis suggests that the reduction of Cr(VI)(aq) to the less toxic solid Cr(III) phase is further promoted by the presence of co-occurring CeO_2 NPs and Fe^{2+} species. This study provides new, mechanistic information on the surface chemistry transformations of CeO_2 NPs in highly competing redox environments. By characterizing the physicochemical properties of both CeO_2 NPs and newly formed hybrid NPs which form during redox reactions with Fe^{2+} and Cr(VI), we provide a basis for understanding the fate and transport of CeO_2 NPs in the environment.

ACKNOWLEDGMENTS

This work is supported by the NSF Environmental Chemical Science (ChE-1214090) grant, and Ray's Environmental Protection Agency STAR Fellowship. The authors would like to acknowledge support from Washington University's Institute of Materials Science & Engineering (IMSE) for the use of TEM and XPS. XAS work was performed at GeoSoilEnviroCARS (Sector 13), Advanced Photon Source (APS), Argonne National Laboratory. GeoSoilEnviroCARS is supported by the National Science Foundation-Earth Sciences (EAR-1128799) and Department of Energy-GeoSciences (DE-FG02-94ER14466). We appreciate constructive suggestions from Dr. Doyoon Kim and other colleagues in the Environmental NanoChemistry Lab (ENCL) at WUStL.

REFERENCES

1. I. Celardo, M. De Nicola, C. Mandoli, J. Z. Pedersen, E. Traversa and L. Ghibelli, Ce^{3+} Ions Determine Redox-Dependent Anti-apoptotic Effect of Cerium Oxide Nanoparticles, *ACS Nano*, 2011, **5**, 4537-4549.
2. C. Xu and X. Qu, Cerium oxide nanoparticle: a remarkably versatile rare earth nanomaterial for biological applications, *NPG Asia Mater*, 2014, **6**, 90.
3. C.-H. Wang and S.-S. Lin, Preparing an active cerium oxide catalyst for the catalytic incineration of aromatic hydrocarbons, *Appl. Catal. A-Gen.*, 2004, **268**, 227-233.
4. F. Zhang, S.-W. Chan, J. E. Spanier, E. Apak, Q. Jin, R. D. Robinson and I. P. Herman, Cerium oxide nanoparticles: Size-selective formation and structure analysis, *Appl. Phys. Lett.*, 2002, **80**, 127-129.
5. B. Park, K. Donaldson, R. Duffin, L. Tran, F. Kelly, I. Mudway, J.-P. Morin, R. Guest, P. Jenkinson, Z. Samaras, M. Giannouli, H. Kouridis and P. Martin, Hazard and Risk Assessment of a Nanoparticulate Cerium Oxide-Based Diesel Fuel Additive-A Case Study, *Inhal. Toxicol.*, 2008, **20**, 547-566.
6. F. R. Cassee, A. Campbell, A. J. F. Boere, S. G. McLean, R. Duffin, P. Krystek, I. Gosens and M. R. Miller, The biological effects of subacute inhalation of diesel exhaust following addition of cerium oxide nanoparticles in atherosclerosis-prone mice, *Environ. Res.*, 2012, **115**, 1-10.
7. K. V. Hoecke, J. T. K. Quik, J. Mankiewicz-Boczek, K. A. C. D. Schamphelaere, A. Elsaesser, P. V. d. Meeren, C. Barnes, G. McKerr, C. V. Howard, D. V. D. Meent, K. Rydzynski, K. A. Dawson, A. Salvati, A. Lesniak, I. Lynch, G. Silversmit, B. D. Samber, L. Vincze and C. R. Janssen, Fate and Effects of CeO_2 Nanoparticles in Aquatic Ecotoxicity Tests, *Environ. Sci. Technol.*, 2009, **43**, 4537-4546.
8. J. A. Rodriguez, T. Jirsak, A. Freitag, J. Hanson, J. Larese and S. Chaturvedi, Interaction of SO_2 with CeO_2 and Cu/CeO_2 catalysts: photoemission, XANES and TPD studies, *Catal. Lett.*, 1999, **62**, 113-119.
9. P. Fornasiero, G. Balducci, J. Kašpar, S. Meriani, R. di Monte and M. Graziani, Metal-loaded CeO_2-ZrO_2 solid solutions as innovative catalysts for automotive catalytic converters, *Catal. Today*, 1996, **29**, 47-52.
10. C.-W. Cho, S.-K. Kim, U. Paik, J.-G. Park and W. M. Sigmund, Atomic force microscopy study of the role of molecular weight of poly(acrylic acid) in chemical mechanical planarization for shallow trench isolation, *J. Mater. Res.*, 2006, **21**, 473-479.
11. J. Darab and D. Matson, Continuous hydrothermal processing of nano-crystalline particulates for chemical-mechanical planarization, *J. Electron. Mater.*, 1998, **27**, 1068-1072.
12. S. Seal, S. K. Bose and S. K. Roy, Improvement in the oxidation behavior of austenitic stainless steels by superficially applied, cerium oxide coatings, *Oxid. Met.*, 1994, **41**, 139-178.
13. S. Roure, F. Czerwinski and A. Petric, Influence of CeO_2-coating on the high-temperature oxidation of chromium, *Oxid. Met.*, 1994, **42**, 75-102.
14. L. Limbach, K., R. Bereiter, E. Müller, R. Krebs, R. Galli and W. J. Stark, Removal of oxide nanoparticles in a model wastewater treatment plant: Influence of agglomeration and surfactants on clearing efficiency, *Environ. Sci. Technol.*, 2008, **42**, 5828-5833.

15. M. L. Lopez-Moreno, G. de la Rosa, J. A. Hernandez-Viezcas, J. Peralta-Videa and J. L. Gardea-Torresdey, X-ray Absorption Spectroscopy (XAS) Corroboration of the Uptake and Storage of CeO2 Nanoparticles and Assessment of Their Differential Toxicity in Four Edible Plant Species, *J. Agr. Food Chem.*, 2010, **58**, 3689-3693.
16. M. I. Morales, C. M. Rico, J. A. Hernandez-Viezcas, J. E. Nunez, A. C. Barrios, A. Tafoya, J. P. Flores-Marges, J. R. Peralta-Videa and J. L. Gardea-Torresdey, Toxicity Assessment of Cerium Oxide Nanoparticles in Cilantro (Coriandrum sativum L.) Plants Grown in Organic Soil, *J. Agric. Food Chem.*, 2013, **61**, 6224-6230.
17. S. Majumdar, J. R. Peralta-Videa, J. Trujillo-Reyes, Y. Sun, A. C. Barrios, G. Niu, J. P. F. Margez and J. L. Gardea-Torresdey, Soil organic matter influences cerium translocation and physiological processes in kidney bean plants exposed to cerium oxide nanoparticles, *Sci. Total Environ.*, 2016, **569–570**, 201-211.
18. H.-J. Eom and J. Choi, Oxidative stress of CeO2 nanoparticles via p38-Nrf-2 signaling pathway in human bronchial epithelial cell, Beas-2B, *Toxicol. Lett.*, 2009, **187**, 77-83.
19. M. Auffan, J. Rose, T. Orsiere, M. De Meo, A. Thill, O. Zeyons, O. Proux, A. Masion, P. Chaurand, O. Spalla, A. Botta, M. R. Wiesner and J.-Y. Bottero, CeO2 nanoparticles induce DNA damage towards human dermal fibroblasts in vitro, *Nanotoxicology*, 2009, **3**, 161-171.
20. S. Hussain, F. Al-Nsour, A. B. Rice, J. Marshburn, B. Yingling, Z. Ji, J. I. Zink, N. J. Walker and S. Garantziotis, Cerium Dioxide Nanoparticles Induce Apoptosis and Autophagy in Human Peripheral Blood Monocytes, *ACS Nano*, 2012, **6**, 5820-5829.
21. K. Takahashi and Y. Miura, Electrochemical studies on diffusion and redox behavior of various metal ions in some molten glasses, *J. Non-Cryst. Solids*, 1980, **38-39, Part 2**, 527-532.
22. A. D. Burnham and A. J. Berry, The effect of oxygen fugacity, melt composition, temperature and pressure on the oxidation state of cerium in silicate melts, *Chem. Geol.*, 2014, **366**, 52-60.
23. A. Paul, *Chemistry of Glasses*, Springer Netherlands, 2012.
24. T. N. Rhys-Jones, H. J. Grabke and H. Kudielka, The High temperature oxidation of iron-chromium alloys containing 0.1 wt. % cerium or cerium oxide, *Mater. Corros.*, 1987, **38**, 65-72.
25. Z. Huaiwei and H. Xin, An overview for the utilization of wastes from stainless steel industries, *Resources, Conservation and Recycling*, 2011, **55**, 745-754.
26. M. Elsner, R. P. Schwarzenbach and S. B. Haderlein, Reactivity of Fe(II)-Bearing Minerals toward Reductive Transformation of Organic Contaminants, *Environ. Sci. Technol.*, 2004, **38**, 799-807.
27. T. B. Hofstetter, R. P. Schwarzenbach and S. B. Haderlein, Reactivity of Fe(II) Species Associated with Clay Minerals, *Environ. Sci. Technol.*, 2003, **37**, 519-528.
28. A. G. B. Williams and M. M. Scherer, Spectroscopic Evidence for Fe(II)−Fe(III) Electron Transfer at the Iron Oxide−Water Interface, *Environ. Sci. Technol.*, 2004, **38**, 4782-4790.
29. S. Loyaux-Lawniczak, P. Lecomte and J.-J. Ehrhardt, Behavior of Hexavalent Chromium in a Polluted Groundwater: Redox Processes and Immobilization in Soils, *Environ. Sci. Technol.*, 2001, **35**, 1350-1357.
30. D. L. Sedlak and P. G. Chan, Reduction of hexavalent chromium by ferrous iron, *Geochim. Cosmochim. Acta*, 1997, **61**, 2185-2192.

31. E. J. Tomaszewski, S. Lee, J. Rudolph, H. Xu and M. Ginder-Vogel, The reactivity of Fe(II) associated with goethite formed during short redox cycles toward Cr(VI) reduction under oxic conditions, *Chem. Geol.*, DOI: http://dx.doi.org/10.1016/j.chemgeo.2017.01.029.
32. M. L. Peterson, G. E. Brown, G. A. Parks and C. L. Stein, Differential redox and sorption of Cr (III/VI) on natural silicate and oxide minerals: EXAFS and XANES results, *Geochim. Cosmochim. Acta*, 1997, **61**, 3399-3412.
33. A. Agrawal, V. Kumar and B. D. Pandey, Remediation options for the treatment of electroplating and leather tanning effluent containing chromium—A Review, *Miner. Process. Extr. Metall. Rev.*, 2006, **27**, 99-130.
34. M. B. Hansen, S. Rydin, T. Menné and J. Duus Johansen, Quantitative aspects of contact allergy to chromium and exposure to chrome-tanned leather, *Contact Dermatitis*, 2002, **47**, 127-134.
35. L. F. Cabeza, M. M. Taylor, G. L. DiMaio, E. M. Brown, W. N. Marmer, R. Carrió, P. J. Celma and J. Cot, Processing of leather waste: pilot scale studies on chrome shavings. Isolation of potentially valuable protein products and chromium, *Waste Manage. (Oxford)*, 1998, **18**, 211-218.
36. A. I. Hafez, M. S. El-Manharawy and M. A. Khedr, RO membrane removal of unreacted chromium from spent tanning effluent. A pilot-scale study, Part 2, *Desalination*, 2002, **144**, 237-242.
37. J. Barnhart, Occurrences, Uses, and Properties of Chromium, *Regul. Toxicol. Pharmacol.*, 1997, **26**, S3-S7.
38. A. R. Gonzalez, K. Ndung'u and A. R. Flegal, Natural Occurrence of Hexavalent Chromium in the Aromas Red Sands Aquifer, California, *Environ. Sci. Technol.*, 2005, **39**, 5505-5511.
39. D. Fantoni, G. Brozzo, M. Canepa, F. Cipolli, L. Marini, G. Ottonello and M. Zuccolini, Natural hexavalent chromium in groundwaters interacting with ophiolitic rocks, *Environ. Geol.*, 2002, **42**, 871-882.
40. F. C. Richard and A. C. M. Bourg, Aqueous geochemistry of chromium: A review, *Water Res.*, 1991, **25**, 807-816.
41. X. Liu, J. R. Ray, C. W. Neil, Q. Li and Y.-S. Jun, Enhanced Colloidal Stability of CeO_2 Nanoparticles by Ferrous Ions: Adsorption, Redox Reaction, and Surface Precipitation, *Environ. Sci. Technol.*, 2015, **49**, 5476-5483.
42. P. Wu, G. Zhang, J. Li, H. Lu and W. Zhao, Effects of Fe^{2+} concentration on biomass accumulation and energy metabolism in photosynthetic bacteria wastewater treatment, *Bioresource Technol.*, 2012, **119**, 55-59.
43. A. Guanghua, W. Yong, T. Xiuxiang and C. Yulin, 2011.
44. A. Babuponnusami and K. Muthukumar, Advanced oxidation of phenol: A comparison between Fenton, electro-Fenton, sono-electro-Fenton and photo-electro-Fenton processes, *Chem. Eng. J.*, 2012, **183**, 1-9.
45. J.-H. Sun, S.-P. Sun, M.-H. Fan, H.-Q. Guo, L.-P. Qiao and R.-X. Sun, A kinetic study on the degradation of p-nitroaniline by Fenton oxidation process, *J. Hazard. Mater.*, 2007, **148**, 172-177.
46. S. Esplugas, J. Giménez, S. Contreras, E. Pascual and M. Rodríguez, Comparison of different advanced oxidation processes for phenol degradation, *Water Res.*, 2002, **36**, 1034-1042.

47. R. El Araby, S. Hawash and G. El Diwani, Treatment of iron and manganese in simulated groundwater via ozone technology, *Desalination*, 2009, **249**, 1345-1349.
48. B. J. Merkel, B. Planer-Friedrich and D. Nordstrom, Groundwater geochemistry, *A Practical Guide to Modeling of Natural and Contaminated Aquatic Systems*, 2005, **2**.
49. D. Klauson, S. Preis, E. Portjanskaja, A. Kachina, M. Krichevskaya and J. Kallas, The Influence of Ferrous/Ferric Ions on the Efficiency of Photocatalytic Oxidation of Pollutants in Groundwater, *Environ. Technol.*, 2005, **26**, 653-662.
50. P. Steinmann and W. Shotyk, Ion chromatography of organic-rich natural waters from peatlands V. Fe2+ and Fe3+, *J. Chromatogr. A*, 1995, **706**, 293-299.
51. S. Jessen, F. Larsen, D. Postma, P. H. Viet, N. T. Ha, P. Q. Nhan, D. D. Nhan, M. T. Duc, N. T. M. Hue, T. D. Huy, T. T. Luu, D. H. Ha and R. Jakobsen, Palaeo-hydrogeological control on groundwater As levels in Red River delta, Vietnam, *Appl. Geochem.*, 2008, **23**, 3116-3126.
52. I. Arslan-Alaton, B. H. Gursoy and J.-E. Schmidt, Advanced oxidation of acid and reactive dyes: Effect of Fenton treatment on aerobic, anoxic and anaerobic processes, *Dyes Pigments*, 2008, **78**, 117-130.
53. K. Cirik, N. Dursun, E. Sahinkaya and O. Cinar, Effect of electron donor source on the treatment of Cr(VI)-containing textile wastewater using sulfate-reducing fluidized bed reactors (FBRs), *Bioresource Technol.*, 2013, **133**, 414-420.
54. A. Ž. Gotvajn, T. Tišler and J. Zagorc-Končan, Comparison of different treatment strategies for industrial landfill leachate, *J. Hazard. Mater.*, 2009, **162**, 1446-1456.
55. İ. Gulkaya, G. A. Surucu and F. B. Dilek, Importance of H_2O_2/Fe^{2+} ratio in Fenton's treatment of a carpet dyeing wastewater, *J. Hazard. Mat.*, 2006, **136**, 763-769.
56. R. Kumar, D. Bhatia, R. Singh and N. R. Bishnoi, Metal tolerance and sequestration of Ni(II), Zn(II) and Cr(VI) ions from simulated and electroplating wastewater in batch process: Kinetics and equilibrium study, *Int. Biodeter. Biodegr.*, 2012, **66**, 82-90.
57. A. S. Ellis, T. M. Johnson and T. D. Bullen, Chromium Isotopes and the Fate of Hexavalent Chromium in the Environment, *Science*, 2002, **295**, 2060-2062.
58. M. R. Boni and S. Sbaffoni, The potential of compost-based biobarriers for Cr(VI) removal from contaminated groundwater: Column test, *J. Hazard. Mater.*, 2009, **166**, 1087-1095.
59. C. Oze, D. K. Bird and S. Fendorf, Genesis of hexavalent chromium from natural sources in soil and groundwater, *PNAS*, 2007, **104**, 6544-6549.
60. X. Wu, C. W. Neil, D. Kim, H. Jung and Y.-S. Jun, Co-effects of UV/H_2O_2 and natural organic matter on the surface chemistry of cerium oxide nanoparticles, *Environ. Sci. Nano*, 2018, **5**, 2382-2393.
61. D. Spuhler, J. A. Rengifo-Herrera and C. Pulgarin, The effect of Fe^{2+}, Fe^{3+}, H_2O_2, an the photo-Fenton reagent at near neutral pH on the solar disinfection (SODIS) at low temperatures of water containing *Escherichia coli* K12, *Appl. Catal. B-Environ.*, 2010, **96**, 126-141.
62. N. Unceta, F. Seby, J. Malherbe and O. F. X. Donard, Chromium speciation in solid matrices and regulation: a review, *Anal. Bioanal. Chem.*, 2010, **397**, 1097-1111.
63. T. V. Plakhova, A. Y. Romanchuk, S. N. Yakunin, T. Dumas, S. Demir, S. Wang, S. G. Minasian, D. K. Shuh, T. Tyliszczak, A. A. Shiryaev, A. V. Egorov, V. K. Ivanov and S. N. Kalmykov, Solubility of Nanocrystalline Cerium Dioxide: Experimental Data and Thermodynamic Modeling, *J. Phys. Chem. C*, 2016, **120**, 22615-22626.

64. J. Zhao, B. Li, C. Yang and X. Rao, Application of Ce(IV) in industrial wastewater treatment, *J. Rare Earths*, 2010, **28**, 37 - 39.
65. D. E. Speed, in *Advances in Chemical Mechanical Planarization (CMP)*, Woodhead Publishing, 2016, DOI: http://dx.doi.org/10.1016/B978-0-08-100165-3.00010-3, pp. 229-269.
66. R. J. Hunter and L. R. White, *Foundations of colloid science*, Clarendon Press, 1987.
67. M. Mallet, K. Barthélémy, C. Ruby, A. Renard and S. Naille, Investigation of phosphate adsorption onto ferrihydrite by X-ray Photoelectron Spectroscopy, *J. Colloid Interface Sci.*, 2013, **407**, 95-101.
68. T.-C. Lin, G. Seshadri and J. A. Kelber, A consistent method for quantitative XPS peak analysis of thin oxide films on clean polycrystalline iron surfaces, *Appl. Surf. Sci.*, 1997, **119**, 83-92.
69. M. Mallet, K. Barthélémy, C. Ruby, A. Renard and S. Naille, Investigation of phosphate adsorption onto ferrihydrite by X-ray Photoelectron Spectroscopy, *J. Colloid Interf. Sci.*, 2013, **407**, 95-101.
70. M. Krawczyk, M. Holdynski, W. Lisowski, J. W. Sobczak and A. Jablonski, Electron inelastic mean free paths in cerium dioxide, *Appl. Surf. Sci.*, 2015, **341**, 196-202.
71. N. Fiol, C. Escudero and I. Villaescusa, Chromium sorption and Cr(VI) reduction to Cr(III) by grape stalks and yohimbe bark, *Biores. Technol.*, 2008, **99**, 5030-5036.
72. B. Merkel, J. and B. Planer-Friedrich, *Groundwater Geochemistry: A Practical Guide to Modeling of Natural and Contaminated Aquatic Systems*, Springer Berlin Heidelberg, Berlin, 2 edn., 2008.
73. B. D. B. Aaronson, C.-H. Chen, H. Li, M. T. M. Koper, S. C. S. Lai and P. R. Unwin, Pseudo-Single-Crystal Electrochemistry on Polycrystalline Electrodes: Visualizing Activity at Grains and Grain Boundaries on Platinum for the Fe^{2+}/Fe^{3+} Redox Reaction, *J. Am. Chem. Soc.*, 2013, **135**, 3873-3880.
74. C. M. Hansel, B. W. Wielinga and S. Fendorf, Structural and compositional evolution of Cr/Fe solids after indirect chromate reduction by dissimilatory iron-reducing bacteria, *Geochim. Cosmochim. Ac.*, 2003, **67**, 401-412.
75. L. E. Eary and D. Rai, Chromate removal from aqueous wastes by reduction with ferrous ion, *Environ. Sci. Technol.*, 1988, **22**, 972-977.
76. S. Music, M. Maljkovic, S. Popovic and R. Trojko, Formation of chromia from amorphous chromium hydroxide, *Croat. Chem. Acta*, 1999, **72**, 789-802.
77. *Water Treatment: Principles and Design*, John Wiley & Sons, Inc., 2nd edn., 2005.
78. D. L. Sparks, *Environmental Soil Chemistry*, Elsevier Science, 2013.
79. M. H. Zoellner, G. Niu, J.-H. Jhang, A. Schaefer, P. Zaumseil, M. Baumer and T. Schroeder, Temperature-Dependent Reduction of Epitaxial Ce1-xPrxO2-δ (x = 0-1) Thin Films on Si(111): A Combined Temperature-Programmed Desorption, X-ray Diffraction, X-ray Photoelectron Spectroscopy, and Raman Study, *J. Phys. Chem. C*, 2013, **117**, 24851-24857.
80. KTH, Visual MINTEQ, 2013. Free Version, Department of Land and Water Resources Engineering, https://vminteq.lwr.kth.se/, 2016).
81. B. Morgan and O. Lahav, The effect of pH on the kinetics of spontaneous Fe(II) oxidation by O2 in aqueous solution – basic principles and a simple heuristic description, *Chemosphere*, 2007, **68**, 2080-2084.

LIST OF TABLES

Table 1. Ferrozine method results of available Fe^{2+} ions remaining at the end of the 6 h reaction period. All solutions were prepared using 10 mM NaCl as indicated in Table S1 describing the composition of the reaction systems. Ferrozine method detection limit = 1.0×10^{-6} M Fe^{2+}

reaction system	$[Fe^{2+}]$ (M)	% $[Fe^{2+}]_0$ remaining
1×10^{-4} M Fe^{2+} (initial)	$9.3\times10^{-5} \pm 7.6\times10^{-6}$	100
1×10^{-4} M Fe^{2+} + 1×10^{-6} M $Cr(VI)_{(aq)}$	$4.7\times10^{-5} \pm 8.3\times10^{-5}$	50.7 ± 7.7
1×10^{-4} M Fe^{2+} + 5×10^{-6} M $Cr(VI)_{(aq)}$	$8.9\times10^{-6} \pm 1.0\times10^{-6}$	9.5 ± 4.8
CeO_2+Fe^{2+}	$2.9\times10^{-5} \pm 5.8\times10^{-6}$	30.9 ± 1.2
CeO_2+Fe^{2+}+Cr	$1.9\times10^{-5} \pm 3.4\times10^{-6}$	20.4 ± 2.4
CeO_2+Fe^{2+}+5Cr	(below detection)*	0

*indicates that approximately all aqueous Fe^{2+} and Cr(VI) was oxidized or reduced

Table 2. DPC colorimetric method results of available Cr(VI) remaining at the end of the 6 h reaction period. All solutions were prepared using 10 mM NaCl as indicated in Table S1 describing the composition of the reaction systems. DPC method detection limit = 1.0×10^{-8} M Cr(VI)

reaction system	[Cr(VI)] (M)	% $[Cr(VI)]_0$ remaining
1×10^{-6} M $Cr(VI)_{(aq)}$ (initial)	$1.3\times10^{-6} \pm 3.6\times10^{-7}$	100
5×10^{-6} M $Cr(VI)_{(aq)}$ (initial)	$5.2\times10^{-6} \pm 2.8\times10^{-7}$	100
1×10^{-4} M Fe^{2+} + 1×10^{-6} M $Cr(VI)_{(aq)}$	(below detection)*	negligible
1×10^{-4} M Fe^{2+} + 5×10^{-6} M $Cr(VI)_{(aq)}$	$2.8\times10^{-6} \pm 1.1\times10^{-6}$	2.3 ± 3.4
CeO_2+Fe^{2+}+Cr	(below detection)*	negligible
CeO_2+Fe^{2+}+5Cr	(below detection)*	negligible

*indicates that approximately all aqueous Fe^{2+} and Cr(VI) was oxidized or reduced

LIST OF FIGURES

Figure 1. (A) Sedimentation and (B) dissolution of **CeO_2**, **CeO_2+Fe^{2+}**, **CeO_2+Fe^{2+}+Cr**, and **CeO_2+Fe^{2+}+5Cr** systems as a function of time. Dashed lines indicate the dissolution and sedimentation experiments conducted under aerobic conditions for the **CeO_2** and **CeO_2+Fe^{2+}** systems. The table adjoining Figure 1 contains the zeta potential and pH measurements for each of the 5 reaction systems measured after the first 10 min of reaction, and after 6 h of reaction.

Figure 2. HR-TEM micrographs of (A) **CeO_2**, (B) **CeO_2+Fe^{2+}**, (C) **CeO_2+Fe^{2+}+Cr**, and (D) **CeO_2+Fe^{2+}+5Cr** systems. Arrows in the HR-TEM micrographs indicate the presence of a secondary mineral phase, which was confirmed to be 6LF.

Figure 3. (A) XPS Fe 2p spectra showing increasing 6LF formation with increasing Cr(VI)(aq) concentration and (B) Cr 3d spectra shows the presence of Cr(III) phases in the **CeO_2+Fe^{2+}+Cr**, and **CeO_2+Fe^{2+}+5Cr** reaction systems. (C) Fourier-transformed Fe K-edge spectra with a boxed peak indicating the presence of a $Fe^{III}_{x}Cr^{III}_{(1-x)}(OH)_3$ solid solution phase.

Figure 4. (A) TGA and (B) DTA spectra for the **CeO_2, CeO_2+Fe^{2+}**, **CeO_2+Fe^{2+}+Cr**, and **CeO_2+Fe^{2+}+5Cr** systems. The arrow in the DTA figure at 800 °C indicates the exothermic crystallization of amorphous (i.e., hydroxide or hydrous) phases.

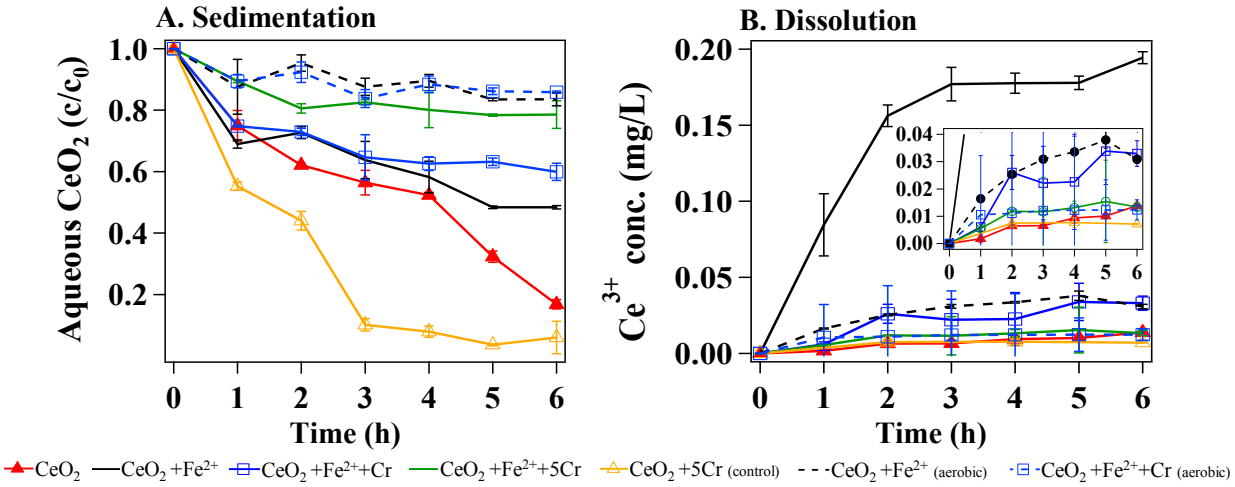

	pH		zeta potential (mV)	
	$t_{0.15\ h}$	$t_{6\ h}$	$t_{0.15\ h}$	$t_{6\ h}$
Bare CeO_2	5.4 ± 0.1	5.4 ± 0.1	16.2 ± 7.3	12.2 ± 7.1
CeO_2+Fe^{2+}	5.1 ± 0.2	4.8 ± 0.1	27.8 ± 3.3	28.1 ± 3.8
CeO_2+Fe^{2+}+Cr	4.8 ± 0.1	4.8 ± 0.1	29.0 ± 2.2	29.7 ± 1.2
CeO_2+Fe^{2+}+5Cr	4.6 ± 0.1	4.3 ± 0.1	31.0 ± 4.8	30.2 ± 0.1
CeO_2+5Cr	5.2 ± 0.1	5.3 ± 0.1	8.9 ± 1.6	-0.5 ± 3.9

Figure 1

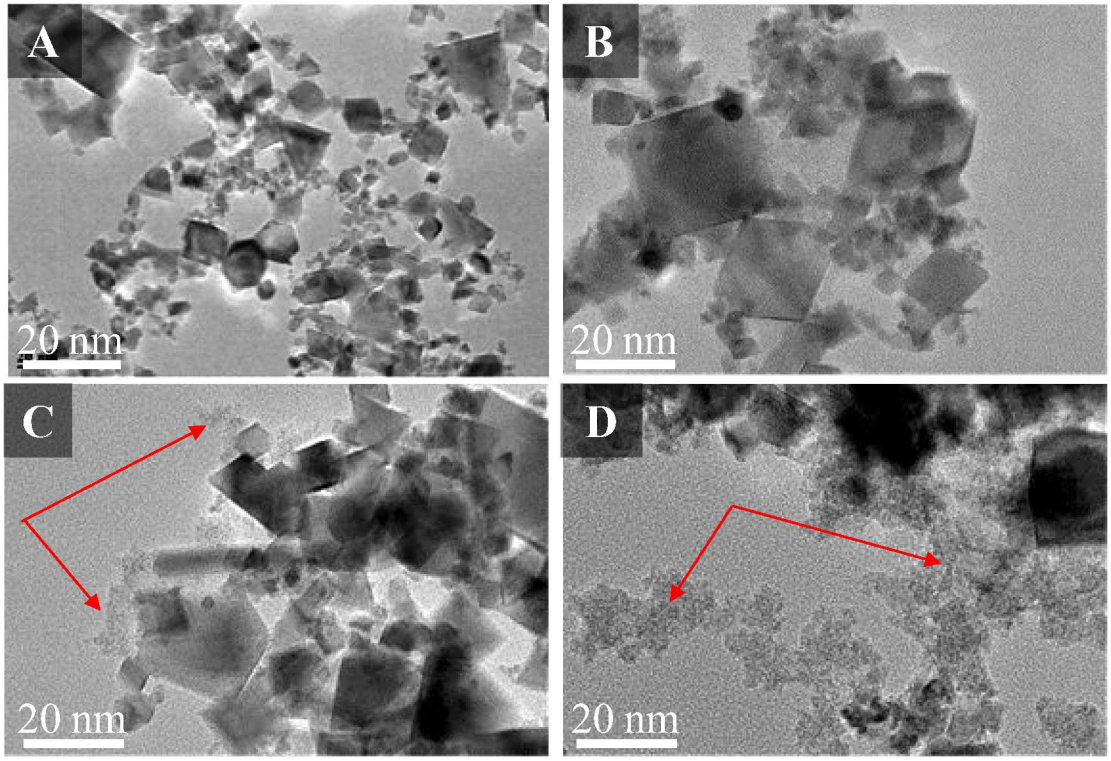

Figure 2

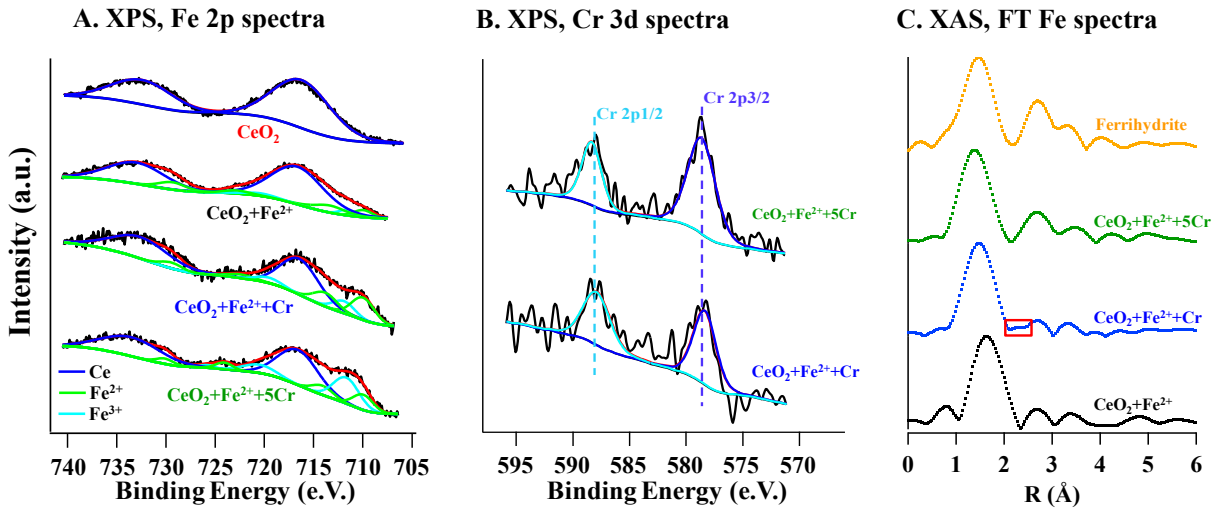
A. XPS, Fe 2p spectra
B. XPS, Cr 3d spectra
C. XAS, FT Fe spectra
Intensity (a.u.)
CeO2
CeO2+Fe2+
CeO2+Fe2++Cr
CeO2+Fe2++5Cr
Ce
Fe2+
Fe3+
740 735 730 725 720 715 710 705
Binding Energy (e.V.)
Cr 2p1/2
Cr 2p3/2
CeO2+Fe2++5Cr
CeO2+Fe2++Cr
595 590 585 580 575 570
Binding Energy (e.V.)
Ferrihydrite
CeO2+Fe2++5Cr
CeO2+Fe2++Cr
CeO2+Fe2+
0 1 2 3 4 5 6
R (Å)

Figure 3

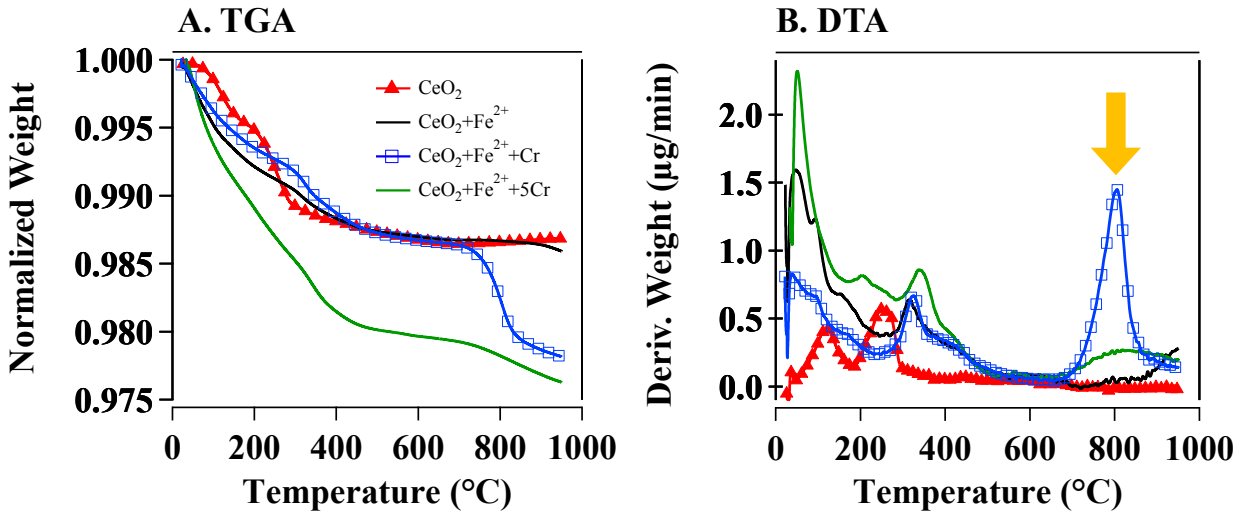
A. TGA
Normalized Weight
1.000
0.995
0.990
0.985
0.980
0.975
0
200
400
600
800
1000
Temperature (°C)
CeO2
CeO2+Fe2+
CeO2+Fe2++Cr
CeO2+Fe2++5Cr
B. DTA
Deriv. Weight (µg/min)
2.0
1.5
1.0
0.5
0.0
0
200
400
600
800
1000
Temperature (°C)

Figure 4

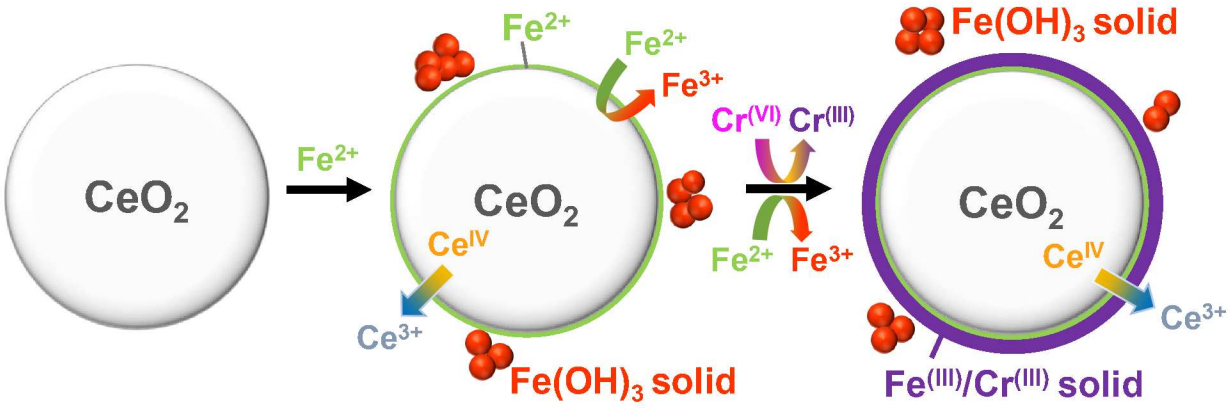

Graphical abstract